JOURNAL OF MATERIALS SCIENCE **33** (1998) 877–886

Processing high-purity and liquid-phase-sintered alumina ceramics using locally synthesized alumina powders

B. A. LATELLA*, B. H. O'CONNOR[‡]
Materials Research Group, Department of Applied Physics, Curtin University of Technology, Perth, WA 6845, Australia

The feasibility of using locally synthesized powders in the development of high-purity and liquid-phase-sintered (LPS) aluminas, for potential use as ceramics in erosive wear environments, was explored. The principal purpose of the project was the development of processing philosophies for alumina-based ceramics that meet the dual, and usually conflicting needs, for improved properties at lower cost, with special attention to the Western Australian mining industry. The incorporation of glassy grain-boundary phases via sintering additives makes the achievement of low-cost LPS aluminas possible, but also threatens to compromise properties. Sintering behaviour, phase assemblage, microstructural evolution and mechanical properties were explored as key variables in this goal. The results indicate that the locally sourced alumina and mineral additives can be combined to produce LPS aluminas which are comparable in mechanical performance to currently-available commercial LPS alumina ceramics. © *1998 Chapman & Hall*

1. Introduction

The use of high-grade technical ceramics for engineering applications, where enhanced mechanical properties and wear-resistance are required, has seen continued growth. The usage of these materials specifically as wear-resistant linings covers a wide range of product forms of which alumina-based ceramics have the most widespread use. Accordingly, the synthesis of low-cost alumina powders, and improvements in the understanding of processing, have created new opportunities for the manufacture of cost-competitive alumina ceramics as wear-resistant components for mineral processing environments.

Alumina-based ceramic oxides are the most versatile and widely-used, traditionally having an Al_2O_3 content ranging from 85–99.9 wt% [1–3]. Materials at the lower end of this range are often categorized as debased aluminas or liquid-phase-sintered (LPS) aluminas. These are obtained by sintering milled alumina powder with moderate amounts of liquid-forming sintering aids, principally comprising a blend of SiO_2, CaO and MgO [1, 2]. The sintering-aid components remain in the cooled product mainly at the grain boundaries, often as a continuous glassy phase, but may also be distributed as intergranular and/or intragranular minor crystalline phases [4]. The use of a liquid phase favours easy and economical processing of LPS aluminas by allowing sintering at lower temperatures and also less-pure aluminas and sintering-aid components to be used [2].

The wear-resistant properties of ceramics have been utilized for many years by the minerals industry to achieve reductions in operating costs. The ease and low cost of processing have made LPS aluminas a popular choice as wear-resistant liners in pipes, chutes, valves, hydrocyclones and pumps [5]. They have also enabled maintenance costs and downtime to be reduced in particular applications by their improved service performance compared to steels and polymers. Ceramic components are now being produced for specialized functions, due to an increasing awareness of the links between processing and microstructure, and between microstructure and properties. This increased specialization has resulted in more careful compositional control and in the deliberate use of microstructural design.

Western Australia is recognized as a region with substantial untapped potential raw materials for the development of advanced ceramic materials through value-added mineral processing. The motivation for this study was that Western Australia had no commercially-exploitable alumina powder sources for use in structural ceramics prior to the study. Ceramic grade alumina powders used in technical ceramics and refractories had been imported even though 15–20% of the Western World alumina is produced locally.

---

* *Present address*: Materials Division, ANSTO, Menai, NSW 2234, Australia.
[‡] Author to whom correspondence should be addressed.

0022–2461 © *1998 Chapman & Hall*

Accordingly, work was conducted in our laboratories to investigate the characteristics of low-soda aluminas produced in Western Australia by Alcoa of Australia Ltd, along with designing a processing protocol to fabricate alumina-based ceramics for use predominantly in high-wear environments. Controlling starting material properties, in order to control reproducibly the sintered microstructures and properties of the end product, was considered to be of vital importance.

The specific aims of the present study were to (i) characterize the synthesized alumina powders (termed A13), (ii) design and develop processing procedures to produce both monolithic and LPS alumina ceramics with appropriate oxide additives from selected raw materials, and (iii) evaluate microstructure and mechanical properties.

The relatively easy, reproducible methodology of the powder processing strategy and the sintering schedules employed to fabricate both the high-purity and LPS aluminas from the locally-synthesized A13 alumina, to accomplish high-density materials with controlled microstructures, are described. Near full densification in the LPS alumina was achieved at lower temperatures than the high-purity alumina due to the influence of the grain-boundary liquid phase. It is shown that the degree of densification and microstructural evolution for both materials depends critically on the sintering temperature and time regime employed. Importantly, the high-purity and LPS aluminas demonstrate equivalent, and in some cases improved, mechanical properties compared to commercially available alumina-based ceramics. The results have important implications for development of low-cost material components using A13 alumina, particularly in the manufacture of debased alumina wear tiles for use as wear-resistant liners in the minerals-processing industry. Opportunities for commercial exploitation of A13 alumina appear to be quite attractive for structural and refractory applications.

2. Experimental procedure

2.1. Materials processing

2.1.1. High-purity alumina

Batches of the starting A13 alumina powder (Alcoa of Australia Ltd, Kwinana Alumina Refinery, Western Australia) doped with 0.03 wt% MgO were prepared. The powders were mixed with deionized water and attrition milled for 4 h in a water-cooled teflon jar containing high-purity alumina grinding media. A combination of 3 wt% polyethylene glycol (PEG) and 0.25 wt% stearic acid were added as binders 0.5 h prior to completion of milling to aid compaction and improve green strength on subsequent pressing. Resultant slurries were separated from the milling media by sieving through a 45 μm sieve. In some instances, portions of slurry were extracted for particle-size analysis during the course of the milling procedure. The slurry mixtures were oven dried for 12 h at ≈ 110° C and then the dried powder cakes were crushed and passed through a 125 μm sieve to break up any hard agglomerates. In a separate trial, a batch of A13 alumina powder was packed in a high-purity alumina crucible and calcined at 1200° C for 5 h in a Kanthal A resistance-heated box furnace. The heating and cooling rates used were 300 and 480 °C h^{-1}, respectively. The calcined batch was then prepared using the same milling procedure.

2.1.2. LPS alumina

These materials were processed in a similar fashion, using the A13 starting alumina with a blend of mineral additives. Formulations comprising a mixture of 84 wt% alumina, 9 wt% kaolinite, 5 wt% talc and 2 wt% calcite powders in deionized water were prepared. The resulting slurries were then attrition milled for 3 h. A 3 wt% addition of PEG was added as a binder 0.5 h prior to completion of milling. The contents were then sieved through 45 μm into a stainless steel bowl from which portions were extracted for particle-size analysis, with the remainder being oven-dried. The resulting powder cakes were crushed and then screened through a 150 μm sieve.

Individual batches of the high-purity and LPS alumina powders were placed in a hardened steel die, lubricated with a mould-release agent (sodium stearate) to lessen sidewall friction and uniaxially dry-pressed at 200 MPa to form pellets 15 mm diameter by 3–7 mm thick. Some larger specimens were also pressed at 50 MPa to form discs 30 mm diameter by 3 mm thick. All pressed green-body specimens were placed in high-purity alumina boats packed with loose bedding alumina powder of the same composition to minimize possible contamination from the furnace atmosphere. Sintering trials were performed in air in a $MoSi_2$ resistance-heated box furnace (Model 46200, Thermolyne). The protocols employed in each case were system-specific, based on thermal analysis data, as summarized below:

(i) High-purity alumina: 120 °C h^{-1} to 450 °C, dwell 1 h
180 °C h^{-1} to 1000–1650 °C, dwell 0.25–6 h
480 °C h^{-1}, cool to room temperature.

(ii) LPS alumina: 120 °C h^{-1} to 450 °C, dwell 1 h
300 °C h^{-1} to 1200 °C, dwell 5 min
180 °C h^{-1} to 1200–1500 °C, dwell 0.25–12 h
480 °C h^{-1}, cool to room temperature.

An isothermal sintering rate study of the LPS alumina involved soaking specimens at 1350 °C for 1 min to 4 h in a custom-made drop bottom furnace (Model HT 06/17, Ceramic Engineering). The specimens were then rapidly quenched on a thick steel plate which was forced-air cooled using a fan.

2.2. Materials characterization

The volume median particle size and particle-size distribution of select powders were measured using laser scattering (Model MS1, Malvern Master Sizer).

Differential thermal analysis (DTA) (Model STA-780, Stanton Red-Croft) measurements were performed on as-received and processed powders. Chemical analysis measurements for the as-received powders were conducted by a National Association of Testing Authorities registered service laboratory, SGS Australia Pty Ltd, using X-ray fluorescence spectrometry and atomic absorption spectroscopy.

Room-temperature X-ray powder diffractometry (XRPD) data were acquired with a Siemens D500 Bragg-Brentano instrument using CuK_α radiation ($\lambda = 0.15418$ nm), produced at 40 kV and 30 mA, over the 2θ range 5°–130°. Crystalline phases in the as-received powders and powdered sintered specimens were identified by a computer-based search-match analysis procedure using the International Centre for Diffraction Data (ICDD) database.

Rietveld analysis [6–8] was used to assay concentrations of the crystalline phases in the starting A13 Al_2O_3 powders and the sintered LPS aluminas. In all cases, absolute values were obtained using data from a reference pure α-Al_2O_3 (UCAR, Union Carbide) powder which served as an external standard. Rietveld refinements were performed with a PC version of the Hill–Howard software [9]. The crystal structure models adopted for the phases present in the starting alumina powders and the sintered materials, namely α-Al_2O_3, θ-Al_2O_3, spinel ($MgAl_2O_4$) and anorthite ($CaAl_2Si_2O_8$) were those published by Lewis *et al.* [10], Zhou and Snyder [11], Megaw [12] and Kempster *et al.* [13], respectively. The parameters adjusted were the phase-scale factors, unit-cell parameters, overall temperature factors, pseudo-Voigt peak profile parameters, third-order polynomial background parameters, and 2θ-scale offset. The final Rietveld scale factors were converted to phase composition (wt%) values using the relation

$$w_{\mathrm{ap}}(\mathrm{wt\%}) = \frac{[s(ZMV)]_{\mathrm{ap}}}{[s(ZMV)]_{\mathrm{ex}}}\left(\frac{\mu_{\mathrm{t}}}{\mu_{\mathrm{ex}}}\right)100 \qquad (1)$$

where s, Z, M, V and μ denote the phase-scale factor, number of formula units per unit cell, formula weight, unit-cell volume and mass attenuation coefficient [14], respectively, of the analyte phase (ap), the external standard (ex) and the bulk material (t).

The green density of compacts was determined by recording the mass and measuring the dimensions of the discs. Shrinkage was determined by the per cent reduction in diameter of the green-body compact to the sintered specimen. The bulk density of the sintered materials was determined using Archimedes' principle [15]. The apparent porosity was determined directly from density measurements. True porosity was calculated from the relative density and theoretical true density values (estimated by rule of mixtures in the LPS alumina).

For preparation of polished surfaces, sintered specimens were cut in half with a diamond saw, mounted in an acrylic thermosetting resin and then routinely polished to 1 μm using diamond paste on silk cloths (oil lubricant). Selected specimens were removed from the mounting resin by heating on a hot plate, placed in high-purity alumina boats and then thermally etched at 1200–1400 °C for a prescribed time based on the composition and sintering temperature of the material. After thermal etching, specimens were gold sputter-coated and microstructures examined with a Philips Jeol JSM-35C scanning electron microscope (SEM). A lineal intercept technique was used to measure grain sizes [16].

2.3. Mechanical property evaluation

Various mounted and polished specimens were indented at a load of 150 N using a Vickers diamond pyramid in order to determine Vickers hardness and fracture toughness (Model 6406, Avery). The lengths of residual impression diagonals and well-defined radial cracks produced from at least five indentations were measured using a calibrated microscope. Hardness was evaluated as the load per contact area [17], and toughness was calculated using the expression developed by Anstis *et al.* [18]. Flexure strength of selected polished specimens were tested in a three-point bend fixture mounted on a universal screw-driven testing machine (Model 1122, Instron). A minimum of four discs were broken in each instance to obtain mean strength values. Elastic properties were derived from pulsed ultrasound measurements of longitudinal and transverse velocities in the materials (HF400, Ultran).

3. Results and discussion

3.1. Raw material characteristics

The measured chemical composition, median particle size and particle-size distribution of two synthesized alumina powders (designated A13-A and A13-B) and selected raw mineral additives used in the LPS alumina composition, are listed in Table I. Slight differences in the levels of impurities were detected in A13-A and A13-B. The mineral additives kaolinite, talc and calcite show higher and moderately different levels of minor impurities, particularly the oxides of Sodium, Iron, Potassium and Titanium. The major cations silicon, calcium and magnesium are of considerable importance as these are the chief constituents for developing a glassy phase. The oxide impurities in the A13 aluminas are considered to be potentially detrimental in the manufacture of a high-purity alumina body as the impurities may (i) segregate to grain boundaries to weaken them, or (ii) combine to form an intergranular liquid film adversely affecting microstructure development by favouring the growth of elongate or plate-like grains [19]. By contrast, the minor impurities from both A13 aluminas in combination with the various mineral additives were expected to have little influence on the processing of LPS aluminas as it allows for less exacting powder preparation so that minor impurities can be tolerated. The particle size and particle size distribution indicate that both alumina powders were coarse, consisting predominantly of weak spherical agglomerates (70–100 μm) made up of individual blocky crystallites in the size range 1–5 μm [20].

TABLE I Chemical composition and particle-size data of the as-received alumina powders and mineral additives

Oxide component (wt%)	A13-A	A13-B	Kaolinite	Talc	Calcite
Al_2O_3	99.2	99.2	25.7	0.76	0.24
SiO_2	0.03	0.03	58.4	59.8	1.03
CaO	0.07	0.07	0.027	0.45	52.2
MgO	0.017	0.017	0.80	31.6	2.0
Na_2O	0.14	0.17	0.27	0.06	0.013
K_2O	0.012	0.012	2.72	0.01	0.024
Fe_2O_3	0.07	0.10	0.99	1.26	0.13
TiO_2	0.02	0.02	1.43	0.03	0.017
P_2O_5	< 0.01[b]	< 0.01	0.05	0.29	0.02
LOI[a]	0.14	0.26	9.6	5.3	44.3
H_2O	0.31	0.29	2.24	0.13	0.2
Total	100.0	100.2	102.2	99.7	100.2
Median particle size, (d_{50}) (μm)	86	97	3.6	11.5	1.8
Particle-size distribution (μm)[c]	100	116	35	38	4.9

[a] Loss on ignition.

[b] Indicates minimum level of detection. Precision of analysis is 0.005%.

[c] Determined from the difference between the 90th percentile and the 10th percentile (d_{90}–d_{10}).

TABLE II Absolute crystalline phase compositions (wt%) for the as-received alumina powders, as determined by Rietveld analysis of the XRPD data

Crystalline phase	A13-A	A13-B	CA13-B[a]
α-Al_2O_3	87.5(1.6)[b]	93.4(1.7)	97.5(2.0)
θ-Al_2O_3	11.5(0.3)	6.4(0.4)	–
Total	99.0(1.6)	99.8(1.8)	97.5(2.0)

[a] A13-B calcined at 1200° C for 5 h.

[b] Concentration values are per cent by weight. Standard deviations are given in parentheses for most significant figures of value.

The phase composition of A13-A and A13-B from Rietveld analysis indicated that both powders were incompletely calcined, consisting of α-Al_2O_3 and a low concentration of θ-Al_2O_3. Table II lists the calculated absolute phase compositions of the two aluminas along with A13-B calcined at 1200 °C for 5 h (denoted CA13-B). The A13-A alumina contains 11.5 wt% θ-Al_2O_3 as opposed to 6.4 wt% in the A13-B. The calcined material showed no evidence of θ-Al_2O_3 consisting solely of α-Al_2O_3 (97.5 wt%).

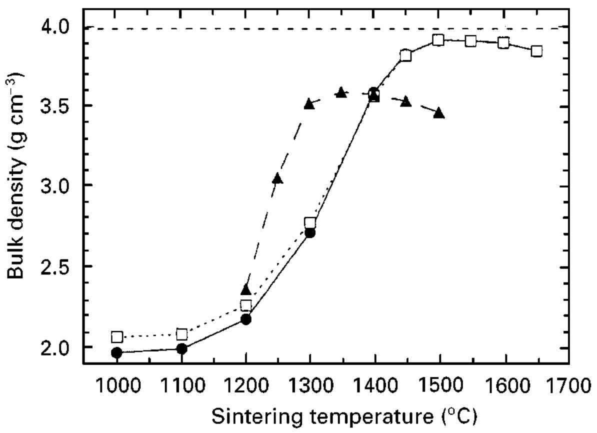

Figure 1 Bulk density of (□) A13-B, (●) CA13-B and (▲) LPS alumina as a function of sintering temperature. (– – –) The theoretical density of α-Al_2O_3 (3.986 g cm^{-3}).

3.2. Processing

The loose alumina agglomerates in the starting A13-A and A13-B powders and the calcined material (CA13-B) resulted in rapid particle-size reduction on attrition milling for 4 h yielding sub-micro metre sized powders ($\approx$0.5 μm) with narrow size distributions. The A13-B alumina was used for processing the high-purity and LPS aluminas. Phase homogeneity was a major issue in the processing of the LPS alumina as incomplete mixing of the powders may adversely affect the sintering behaviour and microstructural homogeneity. It was found that milling the alumina and mineral additives concurrently was the most efficient method in producing homogeneous, well-dispersed narrow sized powder distributions to give optimum fired bulk densities as compared to separate milling of the constituents or only milling alumina. In this instance, the bulk density of the sintered materials proved to be a reliable measure of dispersion and an indirect indicator of particle-size distribution [21].

Fig. 1 shows bulk density versus sintering temperature for A13-B and CA13-B (fixed dwell time of 3 h) along with the LPS alumina (fixed dwell time of 4 h). The theoretical density of α-Al_2O_3 (3.986 g cm^3) has been included as the horizontal dashed line representing the limit to densification for the high-purity aluminas. Both A13-B and CA13-B exhibit a monotonic increase in densification above 1200 °C with matching sintering response at 1400 °C and above. The diametrical shrinkage of the A13-B specimens was higher over the entire temperature range compared to the CA13-B material due to the presence of θ-Al_2O_3 in the starting powder and the lower green density of pressed compacts. These factors had little influence on densification with relative density values $> 97\%$ of the theoretical being achieved above 1500 °C for both

A13-B and CA13-B. The highest bulk density for the LPS alumina was achieved at 1350 °C with a slight reduction occurring at higher temperatures. The decrease in density for the LPS alumina is most likely due to the formation and evolution of gaseous species caused by pore coarsening [22] as evinced by bloating and blistering in some of the materials.

DTA revealed that the melting temperature of the mineral additives comprising kaolinite, talc and calcite, was 1190 °C. Estimates were made of the glass viscosity profile as a function of temperature for the LPS composition using a model developed by Urbain *et al.* [23]. The composition of the glass phase was based solely on the mineral additives, with impurities and any solution effects from the starting alumina being ignored. The viscosity of the glass as a function of temperature is shown in Fig. 2 illustrating a typical exponential decline in viscosity with increasing temperature. The internationally recognized viscosity reference values for the softening and working points used in glass manufacture, $10^{7.65}$ and 10^4 P, respectively, are marked on the plot. The estimated softening and working temperatures obtained from these reference values are 710 and 1110 °C, respectively. The calculated softening point is lower in contrast to the measured value obtained for a similar aluminosilicate glass composition (915 °C) [24]. Yet, the working point estimated is in agreement with the aluminosilicate glass (1190 °C) and the DTA data for the glass composition which showed an endotherm at 1190 °C to signal the onset of melting. The model, although simplistic in nature, gives an indication of the glass viscosity profile with temperature which can be applied to ascertaining changes in densification rates along with providing an indication of the melting conditions and estimates of the working and softening points of a glass.

Fig. 3a shows bulk density as a function of sintering time at various sintering temperatures for A13-B. The characteristic features of the 1550 and 1600 °C firings are the near-theoretical densities achieved after short sintering dwell times with an ensuing decrease at longer times. Specimens sintered at 1500 °C displayed a rapid increase in densification and then a tendency towards saturation with longer dwell time. The same trend was observed in the shrinkage rates as a function of time. The diametrical shrinkages ranged from 20%–22% and the apparent porosities were $< 1\%$.

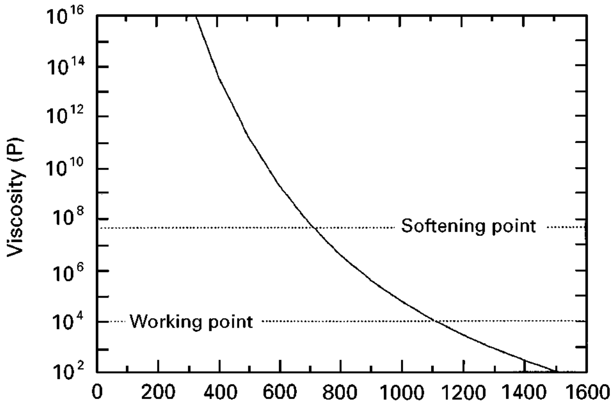

Figure 2 Calculated viscosity profile of the LPS alumina glass phase composition using the model developed by Urbain *et al.* [23].

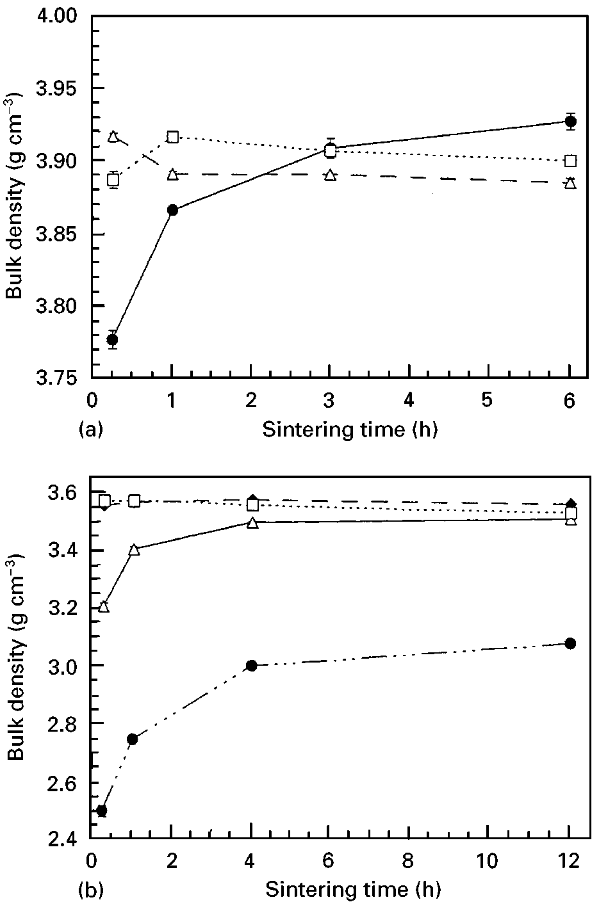

Figure 3 Bulk density as a function of sintering time for (a) A13-B alumina at (●) 1500, (□) 1550 and (△) 1600 °C and (b) LPS alumina at (●) 1250, (△) 1300, (◆) 1350 and (□) 1400 °C.

Sintering of the LPS alumina composition in the range 1250–1400 °C at times of 0.25, 1, 4 and 12 h is illustrated in Fig. 3b. A large step between the 1250 and 1300 °C curves confirmed that a lower viscosity liquid phase improves densification with time (refer to Fig. 2). The curves for the 1350 and 1400 °C firings remained essentially constant with sintering time and diametrical shrinkages being consistently 20%. Apparent porosities ranged from as high as 30% at 1250 °C for 0.25 h to much less than 1% for the specimens sintered at 1350 and 1400 °C. An estimate of theoretical density for the LPS alumina computed by rule of mixtures gave $\rho_{\mathrm{th}} \approx 3.65\ \mathrm{g\,cm^{-3}}$. Therefore, the estimated true porosity values for specimens sintered at 1250 and 1400 °C for 4 h were 18% and 2.5%, respectively.

A plot of diametrical shrinkage as a function of dwell time at 1350 °C in the isothermal sintering kinetics analysis of the LPS alumina is shown in Fig. 4. The shrinkage rate increases rapidly and subsequently declines as the density of the material increases until the curve reaches a saturation point, corresponding to optimum densification. The controlling mechanisms for the LPS alumina composition were evaluated from calculations of the sintering rate (gradients of the

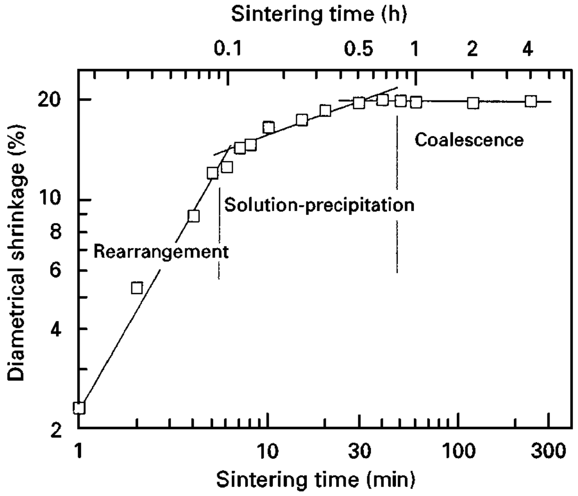

Figure 4 Diametrical shrinkage as a function of sintering time for the LPS alumina at 1350 °C showing three distinct regions related to the densification processes.

TABLE III Experimentally determined gradients from shrinkage data for the isothermal sintering trial of the LPS alumina compared with the mechanism and exponents of time from the Kingery model [25] for liquid-phase sintering

Mechanism	Model	Experimental
Rearrangement	$1 + y$	0.9(1)[a]
Diffusion-controlled	1/3	0.32(6)
Phase boundary-controlled	1/2	–
Coalescence (final)	0	0.003(5)

[a] Standard errors (95% confidence interval) of the least squares gradient given in parentheses are for the least significant digit.

experimental curve), based on comparisons with a model developed by Kingery [25]. Three definite regions were observed in the experimental shrinkage data and linear regression of each gave slopes characteristic of the sintering mechanism. The gradients attained are given in Table III along with the associated mechanism and the exponents of time from the Kingery model.

Ignoring experimental uncertainty, there is slight disagreement in the time exponents between the model and the experimental data for the initial rearrangement stage which depends on the volume fraction of liquid present. This discrepancy may be due to the generally non-spherical particle shape of the starting processed material compared to the ideal spherical particles used in the Kingery model [26]. A substantial portion of the shrinkage curve is best represented by a slope of 0.32, in agreement with the model value of 1/3 confirming that diffusion is the rate-controlling step in the solution–precipitation process. Likewise, a slope which tends towards zero for the final stage (coalescence process) matches the model for the cessation of sintering.

3.3. Phase assemblage

XRPD analysis of selected sintered high-purity alumina specimens fabricated from the A13-B alumina powder showed that the materials were composed almost entirely of corundum (α-Al_2O_3). Some low-level reflections were evident which seemed most likely to be β-Al_2O_3. All LPS alumina specimens were found to be composed of corundum, amorphous glass phase

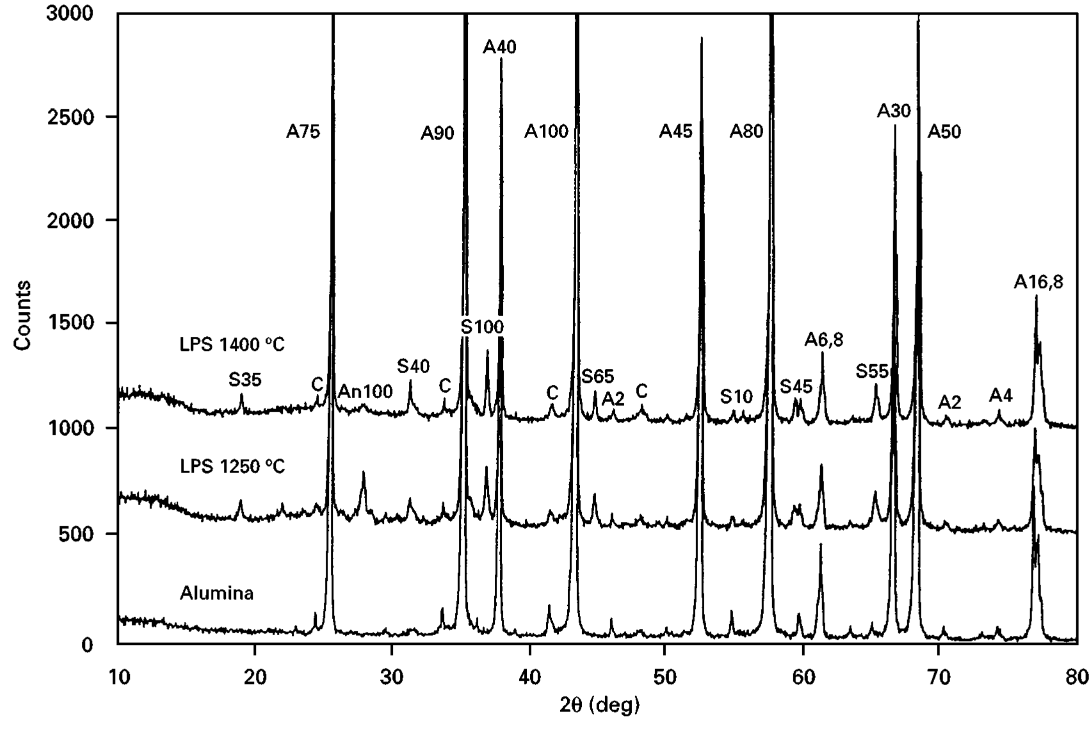

Figure 5 X-ray diffraction patterns ($\lambda = 1.5418$ nm) of the high-purity alumina (1500 °C; 3 h) and the 1250 and 1400 °C LPS aluminas, both sintered for 4 h. The peaks are labelled either A (α-Al_2O_3), S ($MgAl_2O_4$), An ($CaAl_2Si_2O_8$) or C, for "instrumental contaminant", and the associated numbers given in the patterns are the powder diffraction file intensities. The C features correspond to WLα radiation. Patterns are offset for clarity.

and several minor crystalline phases. The presence of the minor crystalline phases, namely, spinel ($MgAl_2O_4$) and anorthite ($CaAl_2Si_2O_8$) were detected over the entire sintering temperature range. These materials had an alumina content ≈ 86 wt%, with ≈ 4 wt% spinel, ≈ 2 wt% anorthite crystalline phases and ≈ 8 wt% glassy phase. Specimens sintered at 1450 and 1500 °C portrayed a diminishing presence of spinel and anorthite concentrations [21]. XRPD plots of the high-purity alumina fired at 1500 °C for 3 h and the LPS alumina fired at 1250 and 1400 °C for 4 h, are presented in Fig. 5.

3.4. Microstructural development

Fig. 6a and b show representative microstructures of high-purity alumina specimens sintered at 1500 °C for 3 and 6 h, respectively. The 3 h firing resulted in specimens having a relative density of $\approx 98\%$, the few pores observed being predominantly at grain-boundary triple points. The grain morphology is generally equiaxed of mean size ≈ 2 µm and with some larger uniform grains (≈ 5 µm) scattered throughout the fine-grained material microstructure. Continued growth and further coarsening of the microstructure occurred following the 6 h firing, showing the presence of large elongated grains (≈ 10 µm wide and ≈ 40 µm long) and irregular-shaped grains within the matrix of fine-grained material 2–5 µm in size. Specimens sintered at 1550 and 1600 °C for different times showed similar trends in terms of microstructural evolution, except that the scale of coarsening increased much more dramatically, as demonstrated in Fig. 7, which displays alumina grain size versus sintering time at each temperature.

There are obvious indications to suggest that coarsening and densification kinetics are intimately linked. This connection is clearly evident in specimens sintered at 1550 and 1600 °C which exhibit a discernible increase in grain size associated with a corresponding drop in bulk density. At these temperatures, the densification rate was lower while rapid grain coarsening occurred (refer to Figs 3 and 8). Correspondingly, observations of the heavily coarsened specimen microstructures, particularly those sintered at 1600 °C, exhibited a higher degree of porosity at the grain boundaries and within grains (Fig. 8). The presence of irregular shaped grains with flat boundaries was evident in many specimens which has been attributed to the formation of a grain-boundary glassy phase presumably arising from the impurity content of the starting powder [27]. This proposition is

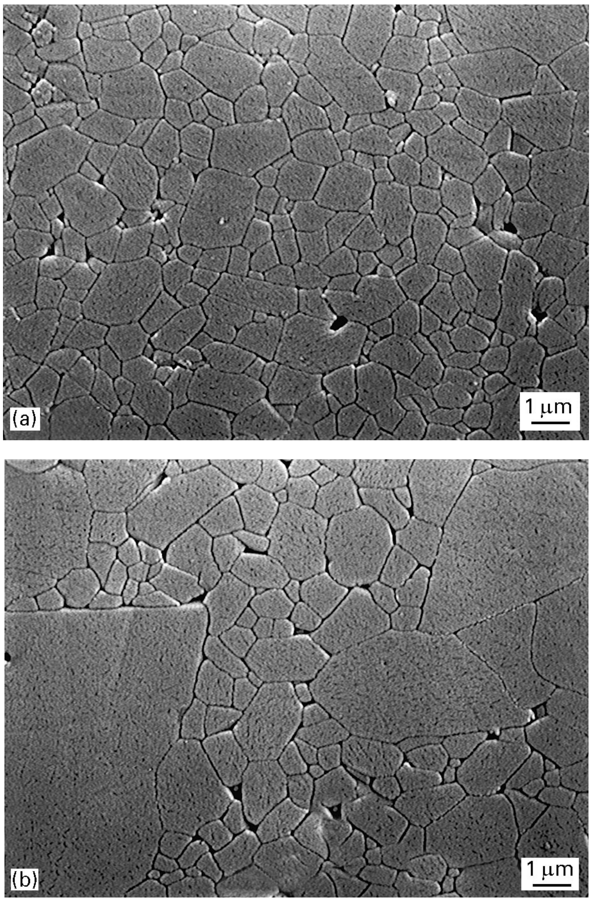

Figure 6 SEM (secondary electrons) microstructures of polished and thermally etched sections of high-purity alumina specimens sintered at 1500 °C for (a) 3 h and (b) 6 h. Specimens were thermally etched at 1320 °C for 0.5 h.

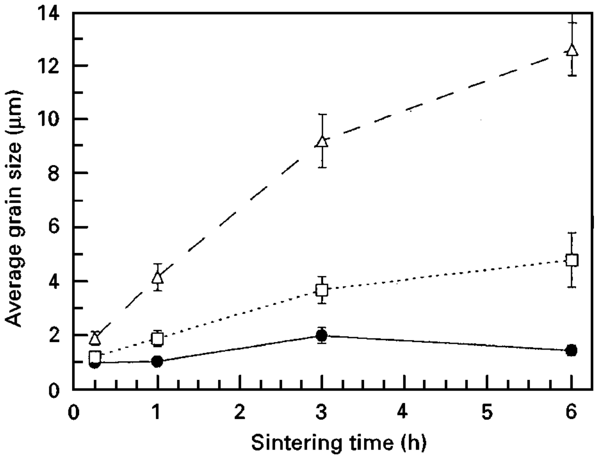

Figure 7 Grain size of the high-purity alumina as a function of sintering time at (●) 1500, (□) 1550 and (△) 1600 °C.

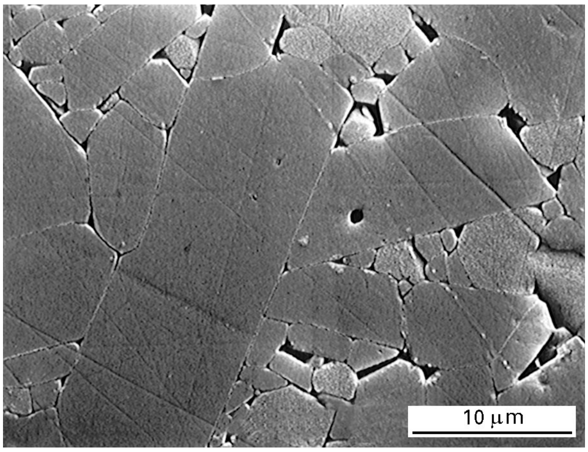

Figure 8 Scanning electron (secondary electrons) micrograph of polished and thermally etched section of the high-purity alumina specimen sintered at 1600 °C for 3 h. The specimen was thermally etched at 1320 °C for 0.5 h.

supported by the reduced effectiveness of MgO additions in suppressing the onset of abnormal grain growth [28].

Microstructural observations of the LPS aluminas revealed only slight differences in the growth of matrix grains and morphology for the sintering temperatures and times examined, apart from subtle changes in the nature and degree of porosity. The material microstructures contained generally small blocky, equiaxed grains. However, no abnormal grain growth was detected. The restricted amount of grain growth implied that the solubility of Al_2O_3 in the glassy phase is limited. Correspondingly, the pores remain attached to the grain boundaries, presumably due to the stabilizing influence of MgO. Some elongate and plate-like grains were observed in specimens sintered at 1400 °C for 12 h, but the average grain size remained quite small, in the vicinity of 3–5 μm, but with a somewhat broader grain-size distribution at longer dwell times. Fig. 9a and b show SEM images of specimens sintered at 1350 °C for 0.25 h and 1400 °C for 4 h, respectively. The glassy intergranular phase was not evident from the scanning electron micrographs as a result of the thermal etching. The orientation of the matrix grains and the advent of some grain dislodgment from the structures by the etching indicates that the glass had completely wet the alumina grains.

3.5. Mechanical properties

Hardness versus sintering time for the high-purity alumina is shown in Fig. 10a. Two main features were evident: (i) a slight increase in hardness for the specimens sintered at 1500 °C reaching a maximum at 1 h, and (ii) a dramatic fall in hardness as a function of sintering time at each temperature, with the rate of decrease being the most substantial in the specimens sintered at 1550 °C. Hardness versus grain size, shown in Fig. 10b, revealed that hardness of the fine-grained aluminas is sensitive to grain size, but insensitive to grain size for the coarser materials. The critical grain size at which this transition occurs is about 4 μm. The data follow a similar trend to that shown by Xu and Jahanmir [29] who proposed a critical grain size between 3 and 9 μm. Hence, grain size has a controlling influence resulting in hardness being sensitive to the scale and heterogeneity of the microstructure.

Fracture toughness measurements made at a load of 150 N were generally restricted to specimens sintered at 1500 °C with fine-grained material microstructures. The measured crack-size values varied considerably (≈ 30%) for individual indents of each specimen, but the overall average K_{IC} computed was 3.3 ± 0.3 MPa m$^{1/2}$. SEM examinations of the residual impressions made by the Vickers diamond pyramid indentor showed that cracking was

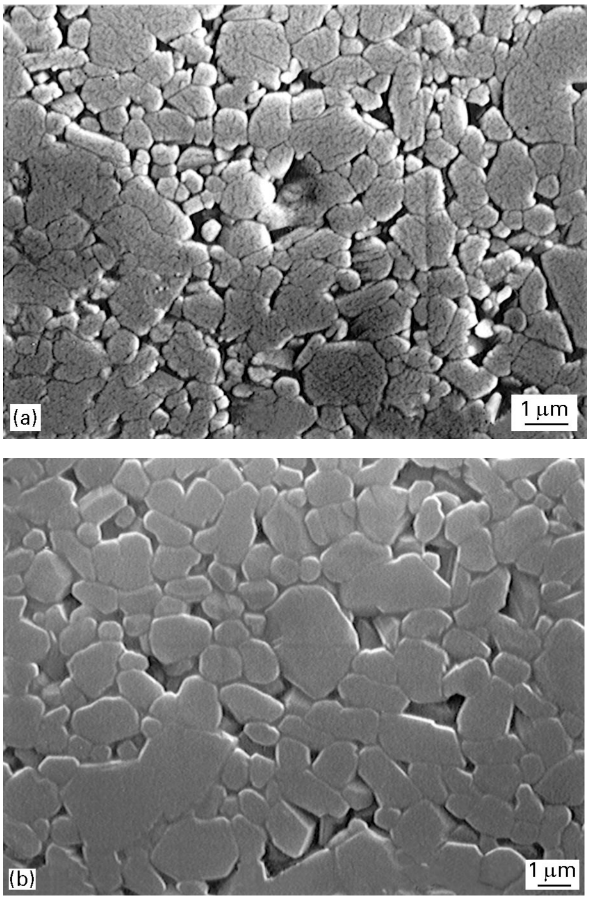

Figure 9 SEM (secondary electrons) microstructures of polished and thermally etched sections of LPS alumina specimens sintered at (a) 1350 °C for 0.25 h, and (b) 1400 °C for 4 h. Specimens were thermally etched at 1200 °C for 1 h. The black regions in the microstructures represent etched glass, porosity and/or grain pullout.

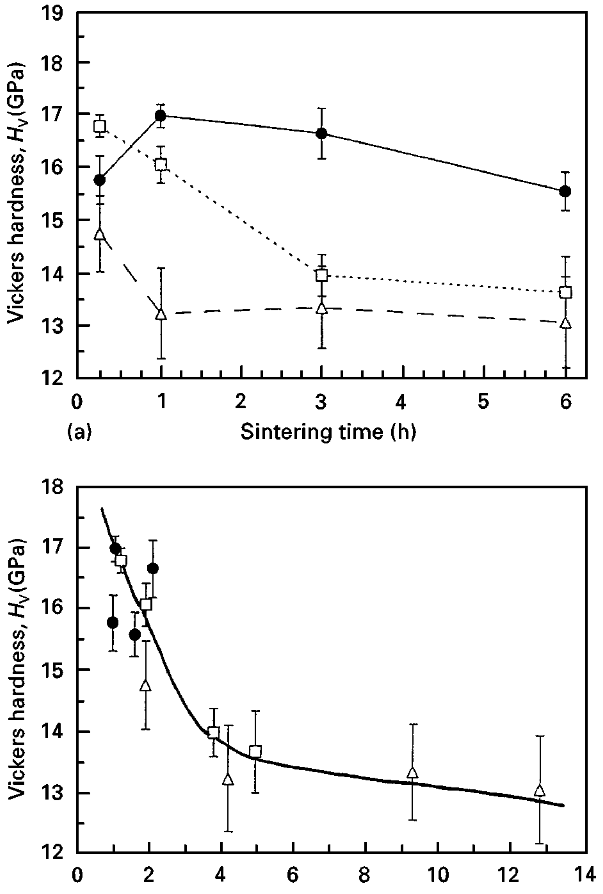

Figure 10 (a) Hardness as a function of sintering time and (b) hardness as a function of grain size for the high-purity alumina at (●) 1500, (□) 1550 and (△) 1600 °C. The solid curve is an empirical fit through the data.

predominantly intergranular with evidence of bridging in the coarse-grained specimens. A great deal of damage and multiple cracking around the immediate indentation sites of these coarse-grained materials was apparent, but no evidence of such damage was observed in the fine-grained specimens, particularly those sintered at 1500 °C, where the fracture mode was primarily transgranular. This is in agreement with the work by Xu and Jahanmir [29] who concluded that the grain-size dependence of hardness correlates with the nature of the damage associated with the indentations.

Hardness as a function of sintering time at each specific temperature for the LPS alumina is shown in Fig. 11. The hardness of the LPS alumina shows a monotonic increase with time at the lower temperatures essentially reaching a maximum saturation point for the 1350 and 1400 °C curves, in accord with bulk density variations (refer to Fig. 3b). Fracture toughness measurements were made on the same materials yielding values ranging from 2.5–3 MPa m$^{1/2}$ but exhibiting no obvious trend with sintering temperature or time. Toughness measurements on the more porous materials were not measured due to problems associated with observing the radial cracks.

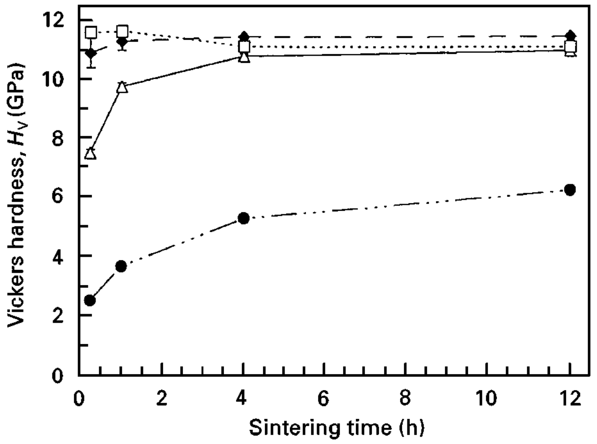

Figure 11 Hardness as a function of sintering time for the LPS alumina composition at (●) 1250, (△) 1300, (◆) 1350 and (□) 1400 °C.

Details of sintering regime, principal microstructural parameters, natural strength, toughness, Vickers hardness number and associated elastic properties of selected LPS materials and a fine-grained high-purity alumina are summarized in Table IV. Included for comparison are data from a Coors AD85 and AD997 material [30]. The mechanical properties of the LPS alumina are generally equivalent to the AD85 material with the high-purity alumina being comparable to AD997. Likewise, it is evident that, as the level of porosity of the LPS materials decreases, there is an analogous improvement in the strength, hardness and elastic moduli. In a separate publication to be published elsewhere, other tests such as indentation-strength, toughness measurements (*T*-curve behaviour) and erosive wear of the materials examined alumina and are shown to exhibit improved wear resistance to several commercially available aluminas currently used as wear components.

4. Conclusions

The feasibility of using newly synthesized, low-cost alumina powders to manufacture alumina-based ceramics has been examined. The principal conclusions from the study are as follows.

1. The processing regime demonstrated that high-purity and LPS alumina ceramics of high densities and fine grain microstructures are achievable using a low-cost, alumina starting material.

TABLE IV Strength, hardness, toughness and elastic properties of the LPS alumina, the high-purity alumina, together with the associated microstructural parameters. Included for comparison are typical properties of Coors AD85 and AD997 aluminas

	LPS Alumina					Al_2O_3	AD85	AD997
	1250 °C, 4 h	1300 °C, 0.25 h	1300 °C, 1 h	1300 °C, 4 h	1400 °C 4 h	1500 °C 3 h		
Grain size (μm)	≈ 1	≈ 1	≈ 2	3	4	2	6.2(6)	2
Density	3.002(3)	3.20(1)	3.40(1)	3.503(3)	3.561(3)	3.91(1)	3.42(2)	3.90(2)
(% th)[a]	(82.2%)	(87.7%)	(93.2%)	(95.9%)	(97.5%)	(98.1%)		(97.8%)
Hardness (GPa)	5.29(5)	7.5(1)	9.8(1)	10.81(8)	11.15(5)	16.7(5)	9.1(1)	16.1(2)
Toughness (MPa m$^{1/2}$)	–	2.5(2)	3.0(2)	2.62(5)	2.4(1)	2.9(2)	3.6(2)	4.3
Strength (MPa)	280(20)	310(57)	412(22)	453(43)	454(23)	594(50)	–	–
E(GPa)	110(15)	127(15)	184(15)	232(15)	268(15)	344(15)	240	372
G(GPa)	49(3)	53(3)	76(3)	96(3)	108(3)	145(3)	98	151
K(GPa)	50(13)	69(13)	108(13)	134(13)	167(13)	183(13)	144	227
v	0.14(2)	0.19(2)	0.21(2)	0.21(2)	0.23(2)	0.19(2)	0.22	0.22

[a] The percentage theoretical density (% th) of the LPS aluminas was based on the estimated true theoretical density of 3.65 g cm^{-3}. The theoretical density for alumina was taken as 3.986 g cm^{-3}. Standard deviations/errors of the mean (95% confidence interval) for the least significant digit(s) are given in parentheses. Standard errors are quoted for the bulk density and hardness values and standard deviations for the strength results. Maximum possible errors are given for the elastic moduli.

2. Near-complete densification of the LPS alumina is achieved at noticeably lower temperatures compared to the high-purity alumina.

3. Experimental observations of the isothermal sintering kinetics of the LPS alumina have shown that it is in satisfactory agreement with theoretical calculations from the Kingery model [24].

4. Microstructural tailoring of the high-purity alumina is easily controlled by sintering temperature and time, although this was rather more insensitive in the coarsening of the LPS alumina.

5. The physical and mechanical properties of the high-density, high-purity and LPS aluminas with fine-grained microstructures are comparable to similar commercial products.

The use of the A13 alumina and mineral additives has important implications in the current environment of manufacturing cost-effective ceramic materials whilst maintaining product integrity and quality. Clearly, there are benefits of using these locally sourced, lower purity materials in the development of low-cost LPS aluminas and other ceramics, being limited only by the requirements and actual applications in which they may be used. This provides an interesting challenge for further processing studies and product development.

Acknowledgements

This work was supported through award to B.A. Latella of an Australian Postgraduate Award PhD scholarship and funding from the Minerals and Energy Research Institute of Western Australia (MERIWA) (Project M207). The authors acknowledge R.J. Stead, Rojan Advanced Ceramics, and J. Lochore, Alcoa of Australia Ltd, for their contributions in management of the MERIWA project.

References

1. G. RICHARDS, *Trans. J. Br. Ceram. Soc.* **80** (1981) 120.
2. R. MORRELL, "Handbook of Properties of Technical and Engineering Ceramics, Part 2 Data Reviews" (HMSO, London, 1987).
3. E. DÖRRE and H. HÜBNER, "Alumina: Processing, Properties, and Applications" (Springer, Heidelburg, 1984).
4. C. A. POWELL-DOGAN and A. H. HEUER, *J. Amer. Ceram. Soc.* **73** (1990) 3670.
5. A. M. MACDONALD, P. J. MUTTON and W. J. SINCLAIR, "Abrasion Resistant Materials for the Australian Minerals Industry," Vol. 2, "Applications for Advanced Ceramics" (Australian Mineral Industries Research Association, Melbourne, 1988).
6. D. L. BISH and S. A. HOWARD, *J. App. Crystallogr.* **21** (1988) 86.
7. B. H. O'CONNOR and M. D. RAVEN, *Powder Diffr.* **3** (1988) 2.
8. R. J. HILL, *ibid.* **6** (1991) 74.
9. R. J. HILL and C. J. HOWARD, "A Computer Program for Rietveld Analysis of Fixed Wavelength X-ray and Neutron Powder Diffraction Patterns", Australian Atomic Energy Commission (now ANSTO) Report no. M112 (Lucas Heights Research Laboratories, NSW, Australia, 1986).
10. J. LEWIS, D. SCHWARTZENBACH and H. D. FLACK, *Acta Crystallogr.* **A38** (1982) 733.
11. R-S. ZHOU and R. L. SNYDER, ibid. **B47** (1991) 617.
12. H. D. MEGAW, "Crystal Structures: A Working Approach" (Saunders, Philadelphia, 1973).
13. C. J. E. KEMPSTER, H. D. MEGAW and E.W. RADOSLOVICH, *Acta Crystallogr.* **15** (1962) 1005.
14. B. D. CULLITY, "Elements of X-ray Diffraction," 2nd Edn (Addison-Wesley, Reading, MA 1978).
15. Australian Standard 1774.5, "Refractories and Refractory Materials – Physical Test Methods. Method 5: The Determination of Density, Porosity and Water Absorption" (Standards Australia, Sydney, 1989) p. 1.
16. J. C. WURST and J. A. NELSON, *J. Amer. Ceram. Soc.* **55** (1972) 109.
17. ASTM Standards E 384, "Standard Test Method for Microhardness of Materials. Section 3 Metals Test Methods and Analytical Procedures," Annual Book of ASTM Standards, Vol. 03.01, "Metals-Mechanical Testing; Elevated and Low-Temperature Tests; Metallography" (ASTM, Philadelphia, PA, 1994) p. 385.
18. G. R. ANSTIS, P. CHANTIKUL, B. R. LAWN and D. B. MARSHALL, *J. Amer. Ceram. Soc.* **64** (1981) 533.
19. H. SONG and R. L. COBLE, *ibid.* **73** (1990) 2077.
20. B. A. LATELLA, B. H. O'CONNOR and R. J. STEAD, *Int. Ceram. Monographs* **1** (1994) 842.
21. B.A. LATELLA, PhD Thesis, Curtin University (1995).
22. A. BELHADJHAMIDA, J. L. JOHNSON, R. TANDON and R. M. GERMAN, *J. Mater Synth Proc.* **1** (1993) 275.
23. G. URBAIN, F. CAMBIER, M. DELETTER and M. R. ANSEAU, *Trans. J. Br. Ceram. Soc.* **80** (1981) 139.
24. O. H. WYATT and D. DEW-HUGHES, "Metals, Ceramics and Polymers" (Cambridge University Press, Bristol, 1974).
25. W. D. KINGERY, *J. Appl. Phys.* **30** (1959) 301.
26. J. W. CAHN and R. B. HEADY, *J. Amer. Ceram. Soc.* **53** (1970) 406.
27. C. A. HANDWERKER, P. A. MORRIS and R. L. COBLE, *ibid.* **72** (1989) 130.
28. C. A. BATEMAN, S. J. BENNISON and M. P. HARMER, *ibid.* **72** (1989) 1241.
29. H. H. K. XU and S. JAHANMIR, *J. Mater. Sci. Lett.* **14** (1995) 736.
30. B. A. LATELLA and R. J. STEAD, in "Proceedings of the International Ceramic Conference Austceram '92", Vol. 1, "Ceramics Adding the Value", edited by M.J. Bannister (CSIRO Publications, Melbourne, 1992) p. 400.

Received 1 May
and accepted 24 September 1997